Breaking Long-Range Order in Iridium Oxide by Alkali Ion for Efficient Water Oxidation

Jiajian Gao,[1] Cong-Qiao Xu,[2] Sung-Fu Hung,[3] Wei Liu,[4] Weizheng Cai,[1] Zhiping Zeng,[1] Chunmiao Jia,[1] Hao Ming Chen,[3] Hai Xiao,[2] Jun Li,[*,2,5] Yanqiang Huang[*,4] and Bin Liu[*,1]

[1] School of Chemical and Biomedical Engineering, Nanyang Technological University, 62 Nanyang Drive, Singapore 637459, Singapore
[2] Department of Chemistry, Tsinghua University, Haidian District, Beijing 100084, China
[3] Department of Chemistry, National Taiwan University, Taipei 106, Taiwan
[4] State Key Laboratory of Catalysis, Dalian Institute of Chemical Physics, Chinese Academy of Sciences, 457 Zhongshan Road, Dalian 116023, China
[5] Department of Chemistry, Southern University of Science and Technology, Shenzhen 518055, China

*Correspondence to: junli@tsinghua.edu.cn (J. Li), yqhuang@dicp.ac.cn (Y. Huang) and liubin@ntu.edu.sg (B. Liu).

Abstract

Oxygen electrochemistry plays a critical role in clean energy technologies such as fuel cells and electrolyzers, but the oxygen evolution reaction (OER) badly restricts the efficiency of these devices due to its slow kinetics. Here we show that via incorporating lithium ion into iridium oxide, the thus obtained amorphous iridium oxide (Li-IrO_x) demonstrates outstanding water oxidation activity with OER current density of 10 mA/cm^2 at 270 mV overpotential for 10 hours of continuous operation in acidic electrolyte. DFT calculations show that lithium incorporation into iridium oxide is able to lower the activation barrier for OER. X-ray absorption characterizations indicate that both amorphous Li-IrO_x and rutile IrO_2 own similar [IrO_6] octahedron units but have different [IrO_6] octahedron connection modes. Oxidation of iridium to higher oxidation states along with shrinkage in the Ir-O bond was observed by *in-situ* X-ray absorption spectroscopy on amorphous Li-IrO_x, but not on rutile IrO_2 under OER *operando* conditions. The much more "flexible" disordered [IrO_6] octahedrons with higher oxidation states in amorphous Li-IrO_x as compared to the periodically interconnected "rigid" [IrO_6] octahedrons in crystalline IrO_2 are able to act as more electrophilic centers and thus effectively promote the fast turnover of water oxidation.

Introduction

Electrochemical water splitting plays an essential role in renewable energy technologies such as fuel cells and electrolyzers, but the sluggish kinetics of the oxygen evolution reaction (OER) badly limit the performance and commercialization of these devices.[1-2] Proton exchange membrane (PEM) electrolyzers offer greater advantages as compared to alkaline electrolyzers such as more compact system design and lower ohmic loss, higher current density and gas purity, larger partial-load range and faster system response.[3] However, one main disadvantage of PEM electrolyzers is the limited choices of materials for the anode catalyst, which has to sustain high electrode potential in acidic environment.[4-5] Currently, the PEM anode catalysts are mainly based on oxides of very scarce ruthenium and iridium noble metals.[6-8] To profit from the advantages of the PEM electrolyzers and promote their large-scale applications, the noble metal amount required in the anode catalyst needs to be drastically reduced. Therefore, lots of efforts have been made to maximize the activity and stability of Ru and Ir based OER catalysts.[4, 9-13] Very recently, a breakthrough was made by Jaramillo and co-workers,[9] who reported that the $IrO_x/SrIrO_3$ film prepared by pulsed laser deposition (PLD) on $SrTiO_3$ (111) substrate could maintain OER specific activity at 10 mA cm^{-2}_{oxide} in 0.5 M H_2SO_4 with an overpotential of only 270 to 290 mV for 30 h. However, the catalyst synthesized by PLD method on single crystal substrate limits its potential application in PEM electrolyzers. Moreover, recent studies have shown that hydrated or hydroxylated amorphous forms of iridium oxide generally exhibit higher OER activity than pristine iridium metal or crystalline rutile-type IrO_2,[14-19] but the underlying origin is unclear and still under debate. Abbott et. al.,[17] considered that the surface of crystalline rutile IrO_2 is

dominated by (110) surface, which has intrinsic low-activity, while Pfeifer et. al.,[15] ascribed the better activity to more electronic defects in amorphous IrO_x. Willinger et. al.,[11] suggested that the interconnected hollandite-like structure in amorphous IrO_x is more active than the rutile structure in crystalline IrO_2. Additionally, debates about the active sites of iridium oxide for OER still exist. For example, some researchers[20-23] stated that iridium species with high oxidation states such as Ir^{5+} or Ir^{6+} act as the active sites of OER, while others[14, 24] suggested that the reactive surface oxygen atoms or species are the key for OER. Thus, to better design high performance OER catalysts in acidic medium, further studies on iridium oxide have to be systematically conducted. Here, our work makes two contributions in acidic water oxidation catalysis: on one hand, we develop a simple method to prepare highly efficient lithium-incorporated amorphous IrO_x OER catalyst in acid media, and on the other hand, we investigate the origin of the activity gap between the amorphous and crystalline iridium oxide for OER by *in-situ* X-ray absorption spectroscopy and DFT calculations.

Results and discussion

Amorphous Li-IrO_x was prepared by reacting $IrCl_3$ with LiOH, while commercial IrO_2 was used as received for comparison. The crystal structures of the iridium oxide catalysts were first examined by X-ray diffraction (XRD) as shown in Figure 1a. All sharp diffraction peaks of commercial IrO_2 can be indexed to the standard PDF card (03-065-2822) of rutile IrO_2. In contrast, the XRD pattern of Li-IrO_x displays very weak and broad peaks, which is very different from that of the commercial IrO_2, indicating the amorphous feature. Commercial IrO_2 (Figure 1b) composes of irregular particles and nanorods with sizes of several hundreds of nanometers, which is the typical morphology of rutile IrO_2.[17] The BET

surface area of commercial IrO_2 measured by N_2 adsorption is 4.3 m^2/g. The as-prepared Li-IrO_x shows a quite different morphology of aggregated and irregular particles with rough surfaces (Figure 1c), having BET surface area of 27 m^2/g. Considering the fact that the oxygen species in iridium oxide are closely related to the OER performance,[14, 24] the activities of the oxygen species in the two catalysts were analyzed by H_2-TPR and the curves are shown in Figure 1d. The reaction of oxygen species with H_2 in rutile IrO_2 starts at around 260 ^oC and ends at 380 ^oC. In contrast, the same reaction on Li-IrO_x starts at 110 ^oC and finishes at 210 ^oC. The lower reaction temperature suggests that the oxygen species are more active in Li-IrO_x than in rutile IrO_2. TEM images of rutile IrO_2 (Figure 1e) show no pores while some pores can be observed in Li-IrO_x (Figure 1f), which may explain the larger surface area of the latter. The selected area electron diffraction (SAED) patterns (insets) show typical diffraction spots for rutile IrO_2 and diffuse rings for amorphous Li-IrO_x, consistent with the XRD results. The Raman spectra (Figure 1g) show similar and typical Ir-O vibrations at E_g, A_{1g} and B_{2g} modes (the peaks of A_{1g} and B_{2g} are overlapped) for both rutile IrO_2 and amorphous Li-IrO_x with Raman shift at 540 and 710 cm^{-1}, respectively.[25] The chemical and electronic states of O and Ir at the surface of the two iridium oxides were analyzed by X-ray photoelectron spectroscopy (XPS). As displayed in Figure 1h, the O 1s XPS spectrum can be deconvoluted into three peaks:[26-28] the lattice oxygen ($O_{Ir\text{-}O}$) at 529.9 eV, the coordinatively unsaturated oxygen or oxygen in hydroxyl group (O_{OH}) at 531.1 eV, and the oxygen in adsorbed water (O_{H_2O}) at 532.6 eV. The peak area percentage of $O_{Ir\text{-}O}$, O_{OH}, and O_{H_2O} in rutile IrO_2 is 39.2 %, 39.7 %, and 21.1 %, respectively, while in Li-IrO_x, O_{OH} is dominant with percentage of as high as 74.6 %. The binding energy of the oxygen species in metal oxide reflects their

interaction with metal cations. Hence, the O 1s spectra indicate higher ratio of the oxygen species on the Li-IrO_x surface that interact weakly with Ir as compared to that on rutile IrO_2, which is consistent with the H_2-TPR results. Figure 1i compares the XPS spectra of Ir 4f, which can be deconvoluted to Ir $4f_{7/2}$ at binding energy of 61.7 eV and Ir $4f_{5/2}$ at binding energy of 64.7 eV with Ir 4f doublet splitting energy of 3 eV for commercial IrO_2, agreeing well with the reported Ir^{4+} XPS spectrum in rutile IrO_2;[15, 26] while the peaks in Ir 4f spectrum of Li-IrO_x clearly shift to higher binding energies with Ir $4f_{7/2}$ at 62.4 eV and Ir $4f_{5/2}$ at 65.4 eV, suggesting that majority of the Ir species on the surface of Li-IrO_x is at +3 valence state.[15, 26]

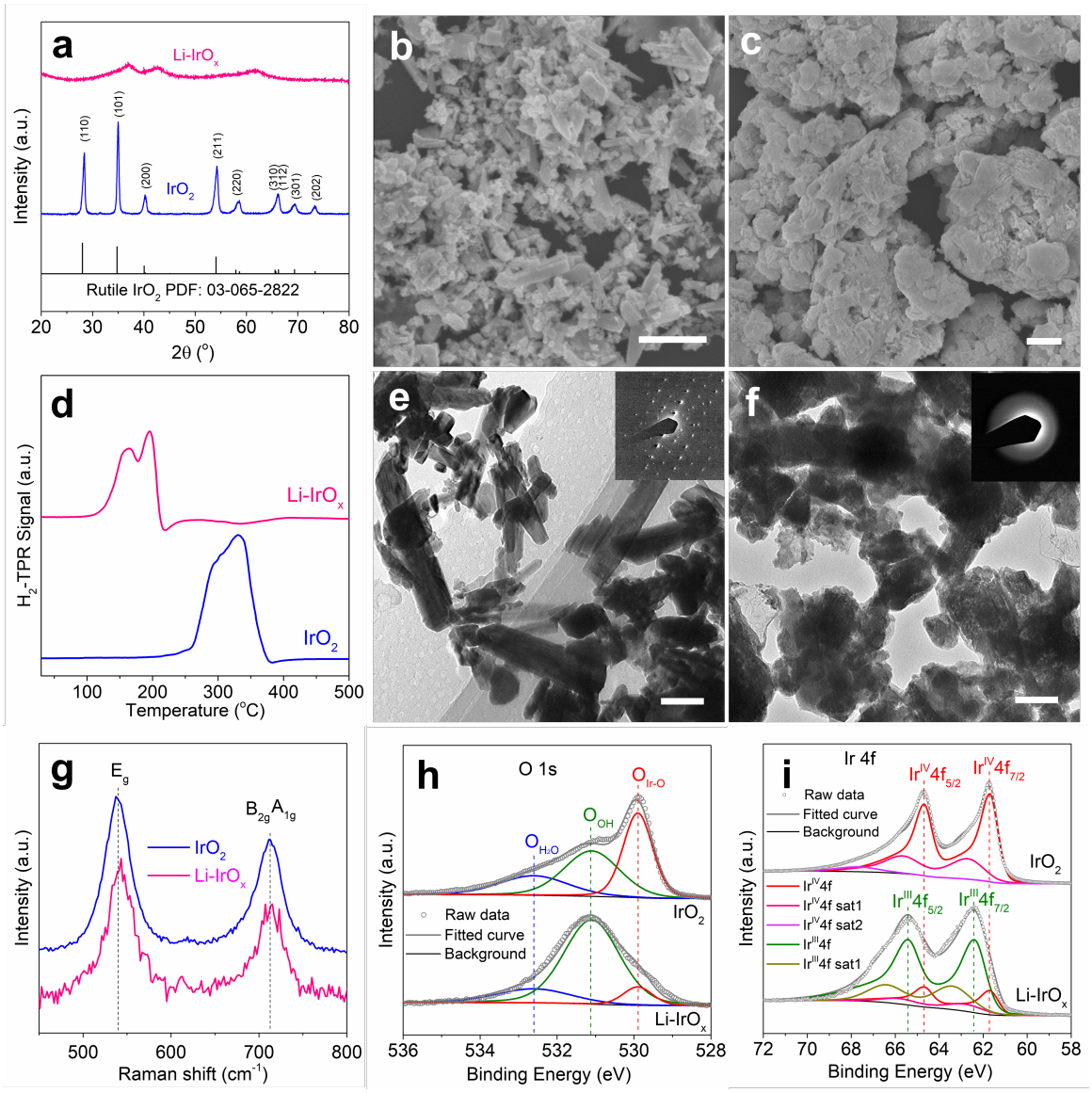

Figure 1. Characterization of rutile IrO_2 and amorphous Li-IrO_x. **a**, XRD patterns of rutile IrO_2 and amorphous Li-IrO_x. **b** & **c**, SEM images of rutile IrO_2 and amorphous Li-IrO_x. Scale bar: 1 μm. **d**, H_2-TPR curves of rutile IrO_2 and amorphous Li-IrO_x. **e** & **f**, TEM images of rutile IrO_2 and amorphous Li-IrO_x. Scale bar: 100 nm. Inset shows the SAED pattern. **g**, Raman spectra of rutile IrO_2 and amorphous Li-IrO_x. **h** & **i**, XPS spectra of O 1s and Ir 4f for rutile IrO_2 and amorphous Li-IrO_x.

High angle annular dark field scanning transmission electron microscopy (HAADF-STEM) was used to further analyze the atomic structure of the two iridium oxides. The contrast in HAADF image comes from the Rutherford scattering between beam electrons

and the Ir (Z =77), O (Z = 16), Li (Z = 3) and H (Z = 1). Here, due to the low scattering power of O, Li and H, only iridium atoms can be observed as bright spots in images generated by the HAADF detector.[11] As displayed in Figure 2a, rutile IrO_2 exhibits clear lattice fringes with distance of 0.26 nm, corresponding to the (011) crystal facets of rutile IrO_2. In contrast, randomly distributed iridium atoms are observable in amorphous Li-IrO_x (Figure 2b), confirming the structural disorder. The insets in Figure 2a and 2b show the corresponding Fourier transform images, which display clear diffraction spots for rutile IrO_2, while only diffuse rings for Li-IrO_x, agreeing well with the XRD and SAED results. Moreover, X-ray absorption near edge spectroscopy (XANES) and extended X-ray absorption fine structure (EXAFS) spectra were collected to examine the oxidation state and atomic coordination of rutile IrO_2 and Li-IrO_x. The Ir L_{III} edge XANES spectra of the two catalysts (Figure 2c) show similar spectral shape and edge position, indicating nearly identical oxidation state (nominal +4) of iridium in the bulk phase. Combined with the XPS results (Figure 1i), it is clear to know that the surface iridium on Li-IrO_x mainly has an oxidation state of +3, while the bulk iridium is in the +4 oxidation state. Furthermore, both EXAFS spectra (Figure 2d) show the first Ir-O shell distance of 1.61 Å in the [IrO_6] octahedron. It should be mentioned that the spectra here were plotted without phase correction, so the distance is a little bit shorter than that of the typical distance of 2.0 Å in [IrO_6] octahedron. Additionally, the second Ir-Ir_I shell and the third Ir-Ir_{II} shell are also clearly observable in rutile IrO_2, while the second and third Ir-Ir shell in Li-IrO_x become very weak. Thus, it is concluded that both rutile IrO_2 and amorphous Li-IrO_x are built from [IrO_6] octahedrons but differ in the way of octahedron connection, which is also consistent with the

HAADF-STEM images. In detail, the [IrO_6] octahedrons are periodically interconnected through corner- or edge-sharing in rutile IrO_2, while those in Li-IrO_x are randomly interconnected and lithium ion is most likely inside the bulk Li-IrO_x, as schematically shown in Figure S1 in supporting information (SI).

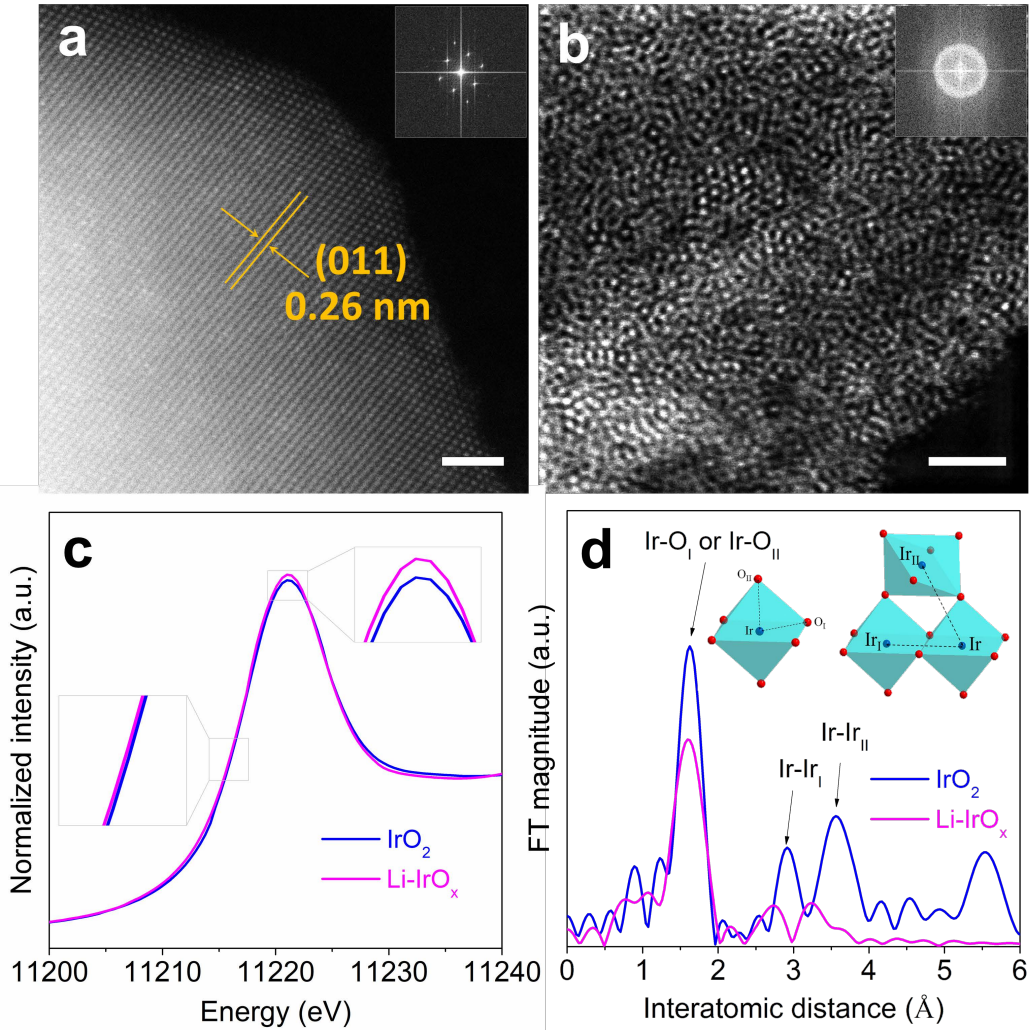

Figure 2. Structural characterization of rutile IrO_2 and amorphous Li-IrO_x. **a** & **b**, HAADF-STEM images of rutile IrO_2 and amorphous Li-IrO_x. Scale bar: 2 nm. Inset shows the corresponding Fourier transform. **c**, XANES spectra for IrO_2 and Li-IrO_x. **d**, EXAFS spectra for IrO_2 and Li-IrO_x.

The OER performance of rutile IrO_2 and amorphous Li-IrO_x were studied on glassy carbon electrode in 0.5 M H_2SO_4 and the results are shown in Figure 3. The linear sweep

voltammetry (LSV) curve in Figure 3a shows that the OER onset overpotential of rutile IrO_2 is around 300 mV and the overpotential to reach the benchmarking 10 $\mathrm{mA\,cm^{-2}_{geom}}$ activity is 435 mV, consistent with the previous reports.[15, 18] In sharp contrast, the amorphous Li-IrO_x exhibits much better OER activity with an onset overpotential of only 200 mV and an overpotential at 10 $\mathrm{mA\,cm^{-2}_{geom}}$ of 290 mV. Figure S2 gives the cyclic voltammetry (CV) curves of Li-IrO_x and IrO_2 to determine the electrochemically active surface area (ECSA).[29] Figure S3 displays the specific activity normalized to surface area, Ir mass, and ECSA as well as turn over frequency (TOF), confirming the superiority of amorphous Li-IrO_x. Moreover, another commercial iridium oxide (IrO_2-AA) with high surface area of 35 m^2/g, which contains significant amount of amorphous phase,[30] and the annealed one (IrO_2-AA-400) were also compared (Figure S4). It can be seen that IrO_2-AA shows higher activity that rutile IrO_2 as shown in Figure S5, agreeing with recent reports.[30-33] However, the normalized activity of Li-IrO_x is still higher compared with IrO_2-AA and IrO_2-AA-400. The Tafel slope for rutile IrO_2 is 68 mV dec^{-1} while that for Li-IrO_x is only 39 mV dec^{-1}, further proving the advantage of Li-IrO_x in OER (Figure 3b). The measured Tafel slope is consistent with the typical reported Tafel slope of iridium oxide in the range of 40 to 70 mV dec^{-1} in acidic media (Table S1 in SI). Additionally, the effect of catalyst loading amount was studied to optimize the overall electrode activity and the data are shown in Figure S6. Higher loading amount leads to higher geometrical area normalized current density at the same potential, but the effect becomes less obvious along with increase in loading amount. A very low overpotential of only 270 mV can be reached at 10 $\mathrm{mA\,cm^{-2}_{geom}}$ with a catalyst loading of 500 $\mu g\,\mathrm{cm^{-2}_{geom}}$. In addition, Li-$IrO_x$ can also reach a metal oxide surface area normalized current of 1

$mA\,cm^{-2}_{oxide}$ at an overpotential of 320 mV and an Ir mass normalized current of 1000 mA/mg_{Ir} at an overpotential of 345 mV. Table S1 presents a detailed activity comparison of reported iridium-based OER catalysts. It is apparent that the amorphous Li-IrO_x catalyst exhibits high OER activity. By comparing the cyclic voltammetry (CV) curves (Figure 3c), amorphous Li-IrO_x displays much stronger redox peaks resulting from the bulk oxidation and reduction of iridium in Li-IrO_x, which will be discussed in detail later. Besides activity, stability is equally important for a catalyst in application. Li-IrO_x was first immersed in 0.5 M H_2SO_4 for 24 h at room temperature under stirring. The CV and LSV curves show negligible changes before and after acid soaking (Figure S7). ICP-OES test shows that the molar ratio of Li : Ir reduced to ~ 0.5 : 1 (Table S2 in SI), namely, some lithium was dissolved from Li-IrO_x, which may mainly come from its surface layers and pores. Then, rutile IrO_2 and amorphous Li-IrO_x were tested at a constant current density of 10 $mA\,cm^{-2}_{geom}$ and the results are shown in Figure 3d. Between the two iridium oxides, rutile IrO_2 cannot maintain stable potential in 0.5 M H_2SO_4, and the result is consistent with the previous report.[34] From the inductively coupled plasma mass spectrometry (ICP-MS) measurements, no iridium could be detected in the electrolyte and on the counter electrode after chronoamperometric test. Thus, the iridium dissolution can be ruled out as the main cause for the rapid deactivation of rutile IrO_2. On the other hand, the amorphous Li-IrO_x exhibits much improved electrochemical stability, which is able to maintain 10, 20 and even 40 $mA\,cm^{-2}_{geom}$ activity at stable potentials during 10 h of continuous operation. In accordance with previous reports,[13, 35-36] dissolution of iridium is inevitable during OER process. Here, ICP-MS test shows that only 3.1 wt% iridium in Li-IrO_x was dissolved after 10 h reaction at 10 $mA\,cm^{-2}_{geom}$. In addition, the molar ratio of

Li : Ir in Li-IrO_x maintained at 0.53 ± 0.13 :1 after the stability test (Table S2). XPS results after reaction show that the surface iridium is partially oxidized to +4 (Figure S8) while HADDF-STEM measurements indicate the maintenance of the amorphous structure of Li-IrO_x (Figure S9). The comparison of CV curves before and after 10 h of continuous operation (Figure S10) shows a slight decrease of redox peak area, which can be mainly attributed to the gradual detachment of catalyst from the rotating disk electrode (RDE) at a high rotation speed of 1600 rpm.

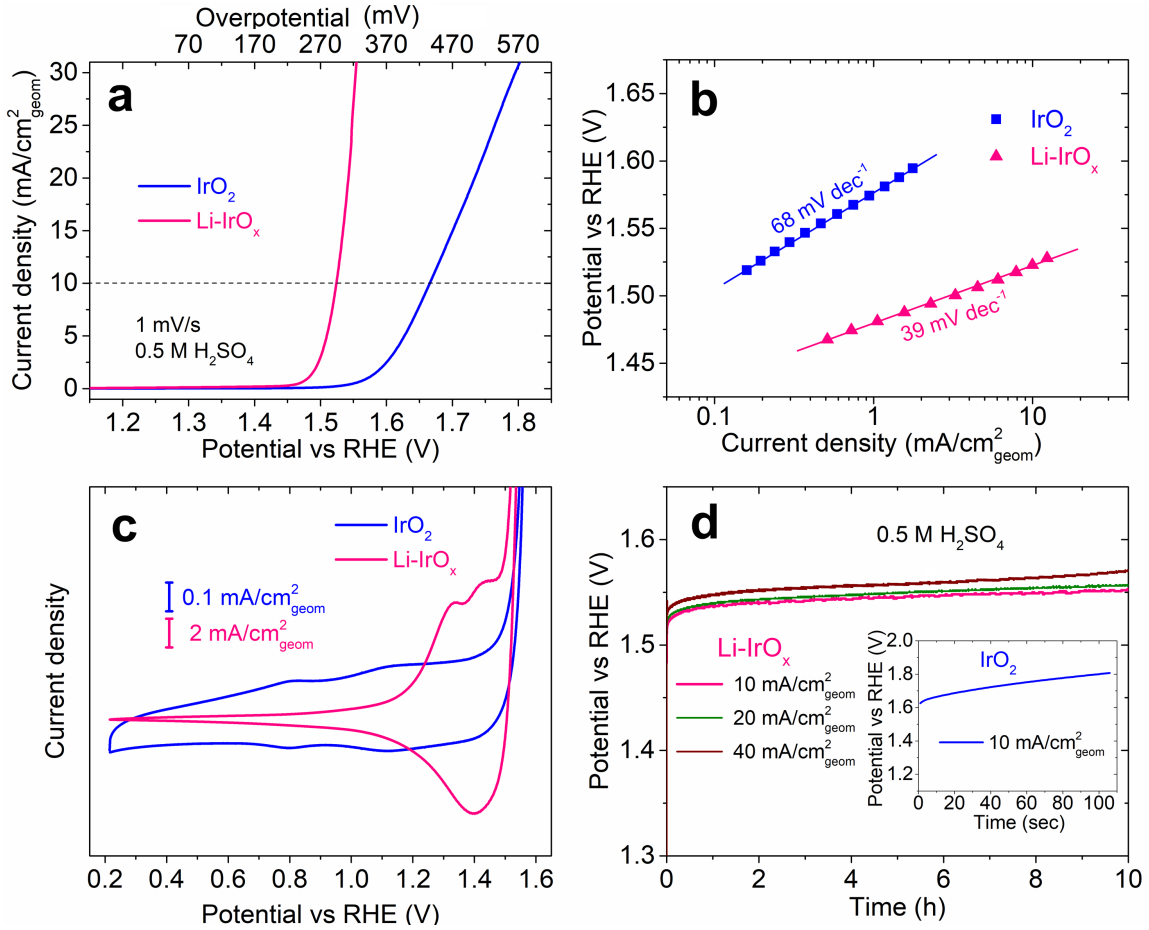

Figure 3. Catalytic performance of rutile IrO_2 and amorphous Li-IrO_x. **a**, LSV curves of rutile IrO_2 and amorphous Li-IrO_x at 1 mV/s with a catalyst loading of 125 $\mu g/cm^2_{geom}$ in 0.5 M H_2SO_4. **b**, Tafel plots for rutile IrO_2 and amorphous Li-IrO_x. **c**, CV curves of rutile IrO_2 and amorphous Li-IrO_x collected at 50 mV/s in the potential range of 0.2 to 1.5 V vs. RHE. **d**,

Chronoamperometry test of amorphous Li-IrO_x at 10, 20 and 40 mA/cm^2_{geom}, inset shows that of rutile IrO_2 at 10 mA/cm^2_{geom}.

To probe the function of lithium in Li-IrO_x for greatly enhanced water oxidation catalysis, LiOH was introduced to rutile IrO_2 at 300 °C (the thus-obtained sample is named as IrO_2-L). After modification, no obvious changes in bulk crystal structure and morphology were observed for IrO_2-L as compared to the starting rutile IrO_2 (Figure S11a and S11b). But, H_2-TPR result (Figure S11c) shows a new small peak in the temperature range of 100 to 150 °C for IrO_2-L, which can be attributed to the active oxygen species formed on the surface, while the bulk reduction of IrO_2-L starts at 250 °C and ends at 380 °C, nearly the same as that of rutile IrO_2. Raman spectra of both IrO_2-L and rutile IrO_2 are nearly identical (Figure S11d). XPS measurements (Figure S12) show no obvious difference for the Ir 4f spectra of IrO_2-L and rutile IrO_2. However, the O 1s spectrum changes obviously for IrO_2-L with increased O_{OH} content, agreeing well with the H_2-TPR result. Additionally, a very thin amorphous layer is observed on rutile IrO_2 particles in IrO_2-L through HAADF-STEM (Figure S13) while XAS shows no structural difference between IrO_2 and IrO_2-L (Figure S14). After modification with LiOH, the overpotential for IrO_2-L to reach 10 $mA\ cm^{-2}_{geom}$ decreases to 395 mV (Figure S15a), accompanying with a decrease in Tafel slope to 52 mV dec^{-1} (Figure S15b). Although both rutile IrO_2 and IrO_2-L show similar CV curves (Figure S15c), the OER stability for IrO_2-L has been significantly improved (Figure S15d). In addition, other alkali ions such as Na^+ and K^+ could also be incorporated into iridium oxide to promote the OER activity (Figure S16).

To further investigate the underlying reason for the activity gap between rutile IrO_2 and amorphous Li-IrO_x, electrochemical AC impedance spectroscopy was performed on rutile IrO_2, IrO_2-L, and Li-IrO_x in the potential range from 1.0 to 1.6 V vs. RHE. Figure S17 shows the corresponding Bode plots. A typical equivalent circuit consisting of the double layer capacitor, adsorption pseudo capacitor, and charge transfer resistor was used to simulate the OER process (Figure S18a).[37-38] The resistance from the electrolyte (R_1) is similar for the three catalysts (Figure S18b), while the charge transfer resistances ($R_{ct} = R_2 + R_3$) are very different but all decrease with increase in applied potential (Figure S18c and S18d). Among the three catalysts, Li-IrO_x has the smallest R_{ct}, matching well with the highest OER activity. The double layer capacitance of IrO_2 is about ten times higher as compared to that of IrO_2-L and Li-IrO_x (Figure S18e). Considering that IrO_2 and IrO_2-L have similar surface area and Li-IrO_x has a surface area six times of them, the main difference of the double layer capacitance should result from the different adsorption capacities and status of the ions on the surface of the catalyst.[39] The capacitance of the adsorption intermediates (Figure S18f) is also well in accordance with the activity of the catalyst, namely, higher activity corresponds to higher adsorption pseudocapacitance.

To monitor the oxidation state change of iridium during OER, *in-situ* XANES spectra of Li-IrO_x under different applied potentials (from 1.05 to 1.45 V vs. RHE) were recorded (Figure 4a). The XANES spectrum collected in air is also included as a reference. After immersing Li-IrO_x into 0.5 M H_2SO_4, no immediate change in the XANES spectrum is noticed. But, the absorption peak of Ir L_{III} edge starts to move towards higher energies (from 11221.0 to 11221.5 eV) when the applied potential is increased from 1.05 to 1.45 V vs. RHE,

which was also observed previously by *in-situ* XAS over electrodeposited disordered iridium oxides[40] or low-crystalline IrO_2[17], indicating an increase of the oxidation state of Ir in Li-IrO_x. The spectrum can be restored back to its initial state when bias is removed. Simultaneously, from *in-situ* EXAFS spectra of Li-IrO_x (Figure 4b), the Ir-O distance shrinks from 1.61 to 1.30 Å if the potential is increased from 1.05 to 1.45 V vs. RHE. The Ir-O distance can also recover to its original length after removing the external bias. In sharp contrast, the *in-situ* XANES and EXAFS spectra (Figure 4c and 4d) of IrO_2-L show no noticeable changes during the entire potential sweeping steps (herein we studied IrO_2-L instead of rutile IrO_2 because of its better OER stability), indicating the maintenance of the rutile structure of IrO_2-L during OER. Considering the much weaker redox peak of IrO_2-L in the CV scan as compared to that of the Li-IrO_x (Figure S15c), we speculate that only very little amount of iridium on the outer surface of IrO_2-L can be oxidized to higher oxidation states during the OER process, and thus cannot be detected by XAS. This is consistent with previous *operando* XAS results, which show that the structure of highly crystalline rutile IrO_2 maintains during OER process.[17] In rutile IrO_2, [IrO_6] octahedrons are periodically linked together, thus making the change of the Ir-O distance (namely, the oxidation state of iridium) very difficult, while in amorphous Li-IrO_x, the [IrO_6] octahedrons are randomly connected and disordered by lithium, and thus their interactions are much weaker and redox behavior would become much easier. Recent studies suggest that the oxidation state turnover is closely related to the high activity of iridium-based catalysts during water oxidation catalysis.[41-42] Here, lithium incorporation is able to break the long-range order of [IrO_6] octahedrons in iridium oxide, which makes the iridium species more flexible during the oxidation-reduction cycles. Furthermore, the easily

oxidizable structure of amorphous Li-IrO_x can also promote intermediate adsorption prior to OER, which shall also accelerate the reaction.[43] In addition, some reaction steps such as the hydroxyl oxidation step (*OH → *O + H^+ + e^-),[44] chemical rearrangement step (*OH' → *OH, *OH' and *OH possess the same chemical structure, but have different energy state),[45] or the O-O bond formation (*O + H_2O → *OOH + H^+ + e^-)[9, 14, 44, 46-47] have been proposed by experiments or calculations as the possible rate or potential determining step in OER on IrO_2. Here, the iridium species in Li-IrO_x are in higher oxidation states and Ir-O distance can be shortened during OER, thus the iridium species are more electrophilic and are able to promote the hydroxyl oxidation and proton release. Moreover, the thus obtained oxygen species (*O) in [IrO_6] octahedrons with shortened Ir-O distance can further act as the electrophilic centers for water molecules to attack to promote O-O bond formation during the catalytic cycles of OER, hence effectively promote the fast turnover of water oxidation. In contrast, the oxidation of iridium is much more difficult due to the "rigid" structure in rutile IrO_2, thereby the kinetics of water oxidation is hindered on its less electrophilic iridium species. This can also be supported by previous reports that IrO_2 with low crystallinity[17] or more disorder[40] as observed by XAS shows higher activity than highly crystalline rutile IrO_2, further suggesting the structural flexibility is very important for the high activity of iridium oxides.

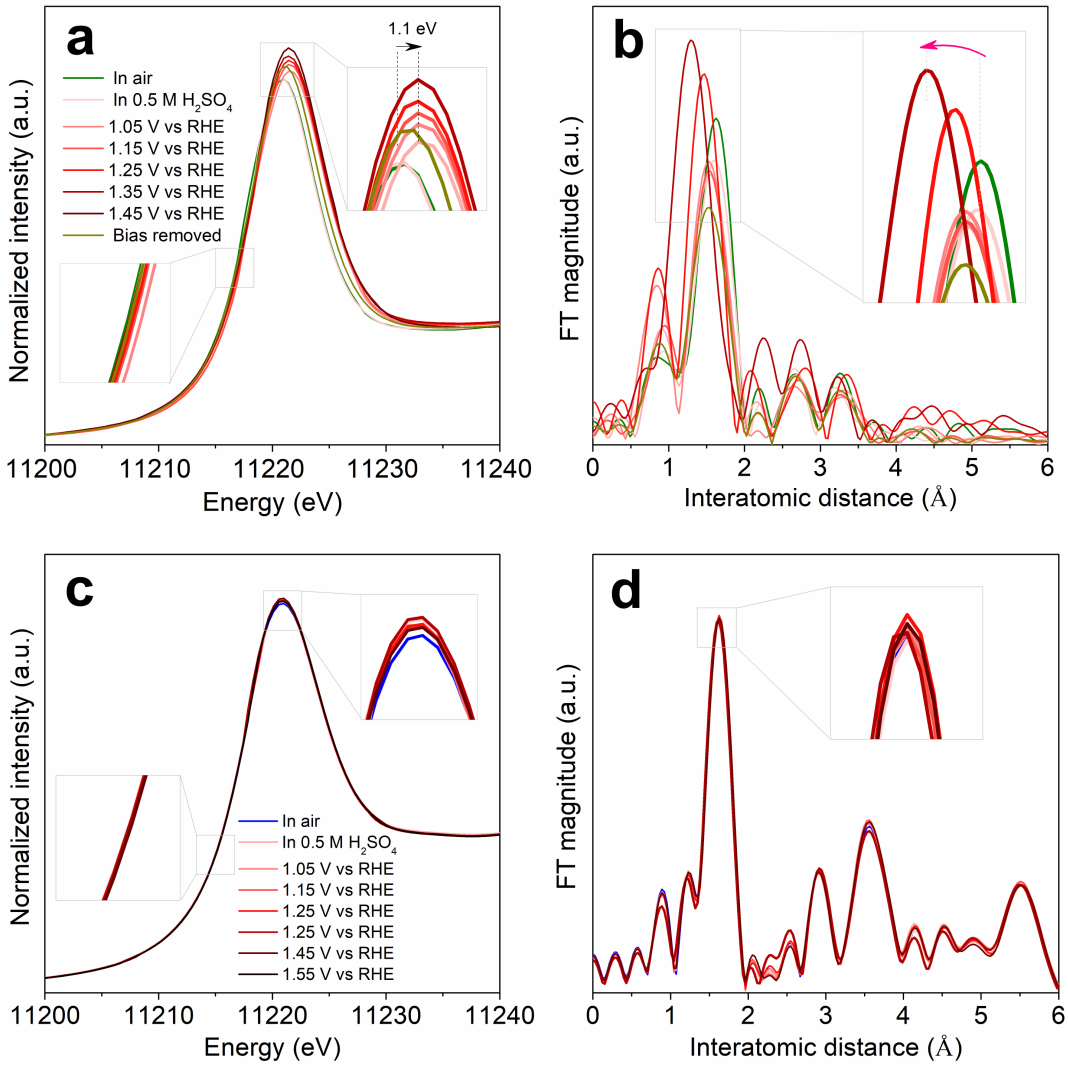

Figure 4. *Operando* X-ray absorption spectroscopy. **a** & **c**, *In-situ* XANES spectra of Li-IrO_x and IrO_2-L. **b** & **d**, *In-situ* EXAFS spectra of Li-IrO_x and IrO_2-L.

DFT calculations were conducted to further understand the origin of the higher OER activity of Li-IrO_x as compared to rutile IrO_2. The thermodynamically stable (110) facet was chosen to model the rutile IrO_2 catalyst.[39] The model for Li-IrO_x was built by replacing some of the IrO_2 units in rutile IrO_2 with Li at a molar ratio of Li : Ir = 0.6 : 1 according to the ICP results. The dangling O was passivated as OH to agree with the O 1s XPS experimental results (Figure 1h), which show lots of OH on the Li-IrO_x catalysts. The final formula of the model for Li-IrO_x is $Li_3Ir_5O_{14}H_8$ (with a molar ratio of formal Ir^{3+} : Ir^{4+} = 3 : 2) and the cell

structure is shown in Figure S19. Our calculations show that the binding energy of Ir 4f core level shifts upward by 0.73 eV from IrO_2 to Li-IrO_x, which is consistent with the experimental results (0.6 eV as shown in Figure 1i). In addition, Figure S20 and Table S3 in SI show a good first shell scattering fit of the EXAFS for Li-IrO_x based on the model proposed. Therefore, the proposed model can well represent the coordination environment and valence state of Ir species in Li-IrO_x.

We assumed a four-step OER mechanism that proceeds through *OH, *O, and *OOH over both rutile IrO_2 (Figure S21) and Li-IrO_x (Figure S22),[47-48] where the asterisk represents the active site (five-coordinated Ir(IV) or Ir(III)). The predicted relative free energies of different intermediates on rutile IrO_2 and Li-IrO_x at three different potentials (0, 1.23 and 1.73 V) are shown in Figure 5. Consistent with previous study,[49] the potential limiting step (PLS) with the highest energy uptake (0.5 eV at U = 1.23 V) over rutile IrO_2 (110) surface is the second proton-couple electron transfer step ($*OH \rightarrow *O + H^+ + e^-$). Incorporation of Li into iridium oxide modifies the intermediate adsorption energies and thus changes the PLS to the last step (with an energy uptake of 0.4 eV at U = 1.23 V). Inasmuch as the DFT calculation conducted here does not predict the oxidation state change of iridium, which has been observed by *in-situ* XAS experiments in Li-IrO_x during the OER process, the effect of the structural flexibility of the amorphous Li-IrO_x during OER process does not seem to be verified by the DFT calculation. However, the calculation has shown that the electronic structure of the Li-incorporated Li-IrO_x system is thermodynamically more beneficial for OER as compared with rutile IrO_2. Assuming that the activation barrier scales with thermodynamics (so-called Brønsted−Polanyi−Evans (BEP) relation) and the kinetic part of the barrier is small, the PLS

can be considered as the rate limiting step.[50] Although it has been reported that reaction mechanism even rate limiting step cannot be deduced directly from Tafel slope as many facts such as the reaction paths, surface coverage of intermediates, overpotential range, et al. can influence its value,[51] it was found that change of rate limiting step to later ones in a mechanism generally decreased the Tafel slope value.[4, 44, 51-52] This trend agrees with the results that the measured Tafel slope decreases from 68 mV dec^{-1} for rutile IrO_2 to 39 mV dec^{-1} for Li-IrO_x. As shown in Figure 5, at the potential of 1.73 V, all the four electron transfer steps over rutile IrO_2 and Li-IrO_x become thermodynamically favorable. However, as observed from the experimental results (Figure 3a), OER on rutile IrO_2 at 1.73 V vs. RHE still proceeds slowly compared with that on Li-IrO_x. As discussed above, the kinetics of hydroxyl oxidation ($*OH \rightarrow *O + H^+ + e^-$) or O-O bond formation over rutile IrO_2 may be hindered by its “rigid” structure; while the “flexible” structure of Li-IrO_x makes the hydroxyl oxidation and the subsequent O-O bond formation proceed fast and thus promote the OER kinetics. Furthermore, the free energy profile of Na-IrO_x as compared to that of rutile IrO_2 was also calculated and is shown in Figure S23. Very similar trend to the Li-IrO_x case is observed for Na-IrO_x, which agrees well with the experimental results (Figure S16), and hence demonstrates the effectiveness of alkali ion incorporation in iridium oxide for promoting the OER catalytic performance. Moreover, the Tafel slopes of Li-IrO_x, Na-IrO_x, and K-IrO_x show changes from 39 mV dec^{-1} for Li-IrO_x, 42 mV dec^{-1} for Na-IrO_x, to 71 mV dec^{-1} for K-IrO_x, suggesting lattice distortion or disorder induced by different alkali ions is distinct and important for the intrinsic activity.

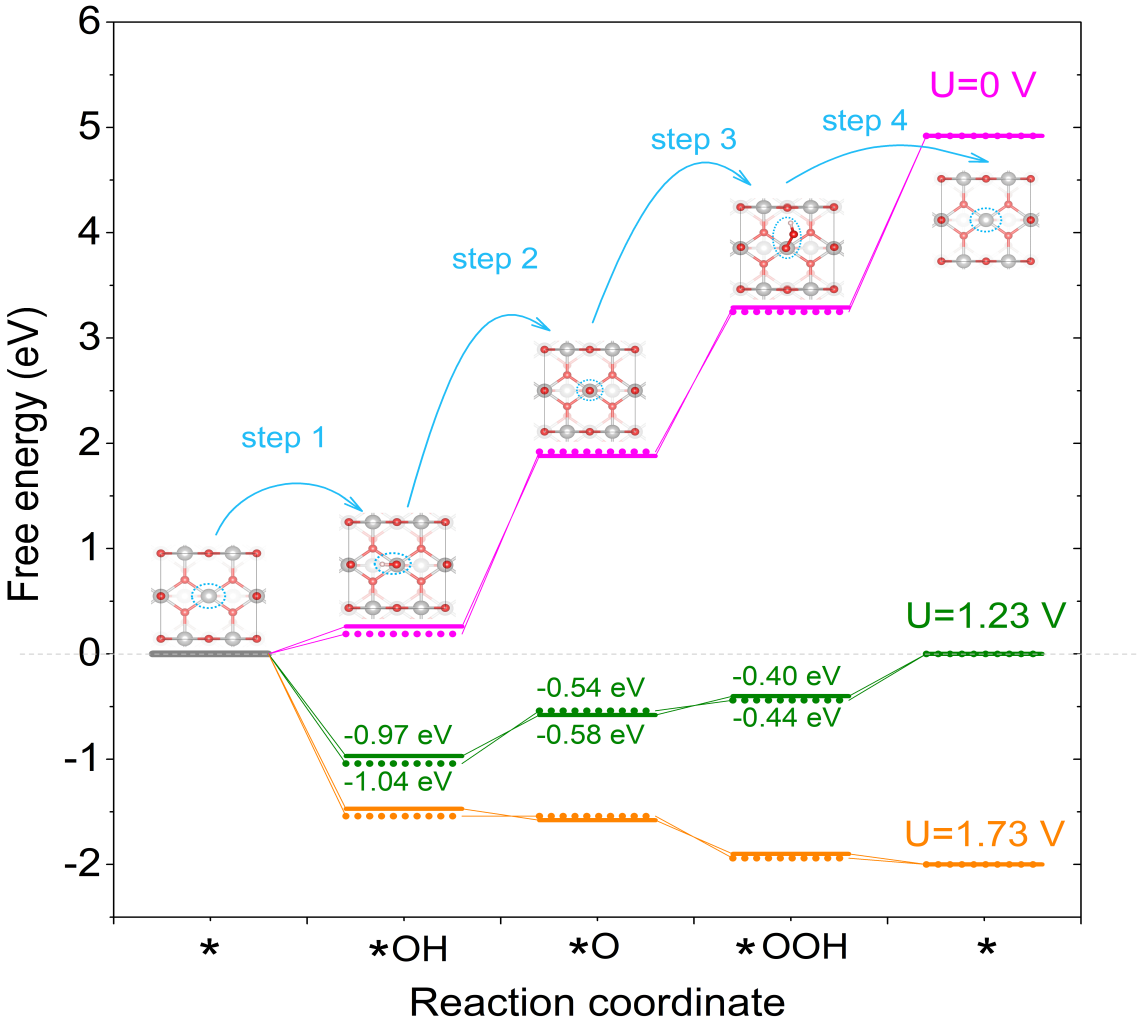

Figure 5. Predicted free energy profiles of OER on rutile IrO_2 (110) surface (dotted line) and Li-IrO_x (110) surface (solid line) at potentials of 0, 1.23, and 1.73 V based on the four-step OER mechanism that proceeds through *OH, *O, and *OOH.

In summary, we have developed a simple method to synthesize highly active and durable amorphous iridium oxide catalyst (Li-IrO_x) for water oxidation in acidic electrolyte. DFT calculations show that OER occurs thermodynamically more favorable on Li-IrO_x than rutile IrO_2. In addition, the iridium in Li-IrO_x with disordered [IrO_6] octahedrons can be easily oxidized during OER along with shrinkage of the Ir-O bond, which is electrophilic and can

effectively promote the hydroxyl oxidation kinetics and the O-O bond formation, eventually promoting the fast turnover of water oxidation.

Method

Catalyst preparation

Chemicals: iridium (III) chloride hydrate ($IrCl_3 \cdot xH_2O$, reagent grade), lithium hydroxide monohydrate ($LiOH \cdot H_2O$, 99.95% trace metals basis), iridium (IV) oxide (IrO_2, 99.9 % trace metals basis, product code: 206237-5G) were purchased from Sigma-Aldrich and used directly without further purification. Commercial iridium oxide with high surface area of 35 m^2/g bought from Alfa Aesar (marked as IrO_2-AA, product no. 43396, Premion®, 99.99% (metals basis), Ir 84.5% min) was calcined at 400 ^oC in static air for 2 h and marked as IrO_2-AA-400. De-ionized water was obtained from Millipore Q water purification system. Lithium incorporated amorphous IrO_x was synthesized as the following: in a typical synthesis, 250 mg of iridium (III) chloride hydrate was dissolved in 5 mL of de-ionized water, followed by adding 5.0 g of $LiOH \cdot H_2O$. Subsequently, the solution was heated to 90 ^oC under stirring to evaporate water and the resultant solid was calcined at 400 ^oC for 2 h under static air. Afterwards, the solid product was washed thoroughly with deionized water and ethanol and dried at 60 ^oC overnight. The obtained catalyst was marked as Li-IrO_x. The synthesis process was repeated three times and the molar ratio of Li to Ir in the synthetic Li-IrO_x determined by ICP-OES is 0.6~0.7 : 1 (Table S2). Na^+ and K^+ incorporated Iridium oxide was prepared by the same method and marked as Na-IrO_x and K-IrO_x respectively. The commercial rutile IrO_2 was calcined at 300 ^oC for 2 h before use and marked as IrO_2. To modify the commercial rutile IrO_2 catalyst: 200 mg of rutile IrO_2 was dispersed into 5 mL of LiOH solution

containing 2.0 g of $LiOH \cdot H_2O$. The suspension was then heated to 90 ^oC to evaporate water under stirring and the obtained solid was further calcined at 300 ^oC for 2 h under static air. Afterwards, the resultant solid product was washed thoroughly with deionized water and ethanol and dried at 60 ^oC overnight (marked as IrO_2-L).

Characterization

Powder X-ray diffraction (XRD) was performed on a Bruker D2 Phaser using Cu Kα radiation with a LYNXEYE detector at 30 kV and 10 mA. The morphological information was examined with field-emission scanning electron microscopy (FESEM, JEOL JSM-6700F). Sub angstrom-resolution high-angle annular dark-field scanning transmission electron microscopy (HAADF-STEM) characterization was conducted on a JEOL JEMARM200F STEM/TEM with a guaranteed resolution of 0.08 nm. The composition of the catalysts was quantified by inductively coupled plasma optical emission spectroscopy (ICP-OES, PerkinElmer), and the dissolved Ir or Li during electrochemical testing was measured by inductively coupled plasma mass spectrometry (ICP-MS, Elan DRC-e). N_2 adsorption-desorption was performed on an Autosorb-6 (Quantachrome) at 77 K. Before analysis, the samples were degassed at 80 ^oC overnight. Brunauer-Emmett-Teller (BET) surface area was calculated in the P/P_o range of 0.05–0.2. Raman spectra were recorded on a Renishaw INVIA Reflex Raman spectrometer using the 514 nm laser as the excitation source. Temperature-programmed reduction with H_2 (H_2-TPR) was carried out on an automated chemisorption analyser (ChemBET pulsar, Quantachrome). Prior to the measurement, about 10 mg of the catalyst was placed in a quartz U-tube and pre-treated in a He stream at 80 °C for 0.5 h, followed by cooling to room temperature. H_2-TPR was conducted in a gas mixture

of 5 vol. % H_2 in Ar at a flow rate of 30 mL/min. The temperature was raised to 500 °C at a ramping rate of 10 °C/min. The amount of H_2 consumption was recorded by a thermal conductivity detector (TCD). XPS measurements were carried out on a Thermofisher ESCALAB 250Xi photoelectron spectrometer (Thermo Fisher Scientific) using a monochromatic Al Kα X-ray beam (1486.6 eV). All binding energies were referenced to the C 1s peak (284.6 eV) arising from the adventitious carbon-containing species. X-ray absorption spectroscopy (XAS) measurements including X-ray absorption near edge spectroscopy (XANES) and extended X-ray absorption fine structure (EXAFS) by employing synchrotron radiation light source were collected in total-fluorescence-yield mode at ambient air in BL-12B2 at SPring-8, Japan Synchrotron Radiation Research Institute (JARSI), in which the electron storage ring was operated at 8.0 GeV. The measurements were made at Ir L_{III}-edge (11215 eV) with the sample held at room temperature. *In-situ* XAS measurements were collected in a specially designed Teflon container with a window sealed by Kapton tape, which was operated in identical conditions as the electrochemical measurements. X-ray could transmit through the tape and electrolyte, so that the signal of X-ray absorption spectroscopy could be collected in total-fluorescence-yield mode in BL-12B2 at SPring-8, JARSI.

Electrochemical measurements

The electrochemical performance of various iridium oxide catalysts was evaluated in a three-electrode configuration with platinum plate (1 cm × 2 cm) as the counter electrode and Ag/AgCl electrode with saturated KCl salt bridge as the reference electrode on a rotating disk electrode (RDE) setup (Pine Research Instrumentation, USA) and a CHI (660E) potentiostat. A reversible hydrogen electrode (RHE) was made with two Pt plates as working and counter

electrodes to calibrate the Ag/AgCl electrode and H_2 is bubbled over the working electrode. To perform the calibration, the clean Pt electrode is cycled at a scan rate of 10 mV s^{-1} around the expected value for the RHE in 0.5M H_2SO_4. Then the open circuit potential is measured (−0.215 V) as shown in Figure S24. All potentials reported herein are referenced to the (RHE) scale following: $E_{vs\ RHE} = E_{vs\ Ag/AgCl} + 0.215$ V. The overpotential η is calculated by: $\eta = E_{vs\ RHE} - 1.23$ V. To prepare the working electrode, the catalyst ink that was prepared by ultrasonically mixing 10 mg of the iridium oxide catalyst, 0.98 mL of Milli-Q H_2O (15 MΩ), 0.98 mL of isopropyl alcohol, and 40 μL of 5 wt. % D520 Nafion dispersion solution was drop-casted on freshly polished glassy carbon electrode (5 mm diameter, Pine). The RDE was kept a rotation speed of 1600 rpm for all electrochemical measurements. Before electrochemical data collection, the working electrode was cycled for several times between 0.2 and 1.5 V vs. RHE at a scan rate of 50 mV s^{-1} to achieve a stable performance. Cyclic voltammograms (CVs) were recorded in the potential range of 0.2 − 1.55 V vs. RHE at 50 mV s^{-1}. Linear sweep voltammetry (LSV) curves were recorded at a scan rate of 1 mV s^{-1} with solution Ohmic drop correction. The measurements were repeated three times with catalysts prepared in different bathes and the overpotential deviation was within ±3 mV at 10 mA cm^{-2}_{geom}. Tafel plots were constructed by sweeping the electrode potential from high to low values across the linear Tafel region. At each potential, current density was collected for 30 − 60 s to ensure steady state. The electrochemically active surface area (ECSA) of each catalyst is estimated through the pseudocapacitive charge according to the reported method.[29] The pseudocapacitive charge of each catalyst was determined by integrating the CV from 0.3 V to 1.25 V and dividing by the scan rate of 50 mV/s.[22, 29] Then, an ECSA-charge constant of

1681 cm^2/C was used to calculate the ECSA.[29] Electrochemical AC impedance spectroscopy measurements were performed in the frequency range from 50 kHz to 0.5 Hz with an amplitude of 10 mV at various potentials. All measurements were repeated at least two times to ensure reproducibility. Considering the fact that different catalysts have different surface area and iridium content, the reported current densities were either normalized to the geometrical surface area of the glassy carbon electrode ($mA\,cm_{geom}^{-2}$), the BET surface area of the catalyst ($mA\,cm_{oxide}^{-2}$), the ECSA of the catalysts ($mA\,cm_{ECSA}^{-2}$), the amount of the iridium content in the catalyst ($mA\,mg_{Ir}^{-1}$), or turn over frequency (TOF) for fair comparison.

Theoretical and computational methods

Spin-polarized density functional theory (DFT) calculations were performed using the Vienna Ab-initio Simulation Package (VASP)[53-54] with the projector augmented wave (PAW) method[55] and a cutoff kinetic energy of 400 eV for plane-wave basis set. The generalized gradient approximation with PBE functional[56] was used. An energy difference within 1.0×10^{-5} eV and force threshold of 0.02 eV/Å for the maximal component were set as the convergence criteria to solve for wavefunctions and geometry optimization, respectively. The reciprocal Brillouin zones were sampled by the Γ-centered Monkhorst-Pack scheme[57] with resolutions of around $2\pi \times 1/40$ $Å^{-1}$. The XPS Ir 4f binding energy shift was approximated by the change of Ir 4f core level from the ground state calculations, and the level splitting from spin-orbit coupling was neglected.

The optimized lattice parameters of bulk rutile IrO_2 were determined to be a = 4.503 Å and c = 3.177 Å, which are in good agreement with experimental results.[58] The models for Li- and Na-incorporated IrO_x (Figure S19) were built by substituting IrO_2 units with Li or Na

atoms to reach a atomic ratio of Li/Na : Ir = 0.6 : 1, close to the experimental value (0.6~0.7 : 1). Additionally, as the XPS of O 1s shows significant increase of hydroxyl group, we passivated the dangling O atoms by OH groups, leading to the final formula of $M_3Ir_5O_{14}H_8$ (M = Li, Na). All (110) facets were modeled by 2 × 2 supercells and four-layer slabs, with vacuum regions of 15 Å. The bottom two layers were fixed to the bulk positions, while the top two layers were allowed to relax. Previous works proved that the oxygen coupling (*O + *O) reaction is less favorable than the formation of *OOH intermediate.[46, 59] Meanwhile, our DFT calculations show that the *OOH intermediate is more stable than the *O + *O intermediate with a free energy difference of 0.36 eV at the Li-IrO_x (110) surface. Consequently, it is assumed that the OER involves the following four steps, where the symbol "*" represents the active site (five-coordinated Ir(IV) or Ir(III)).

$$* + H_2O \rightarrow *OH + H^+ + e^- \quad (1)$$

$$*OH \rightarrow *O + H^+ + e^- \quad (2)$$

$$*O + H_2O \rightarrow *OOH + H^+ + e^- \quad (3)$$

$$*OOH \rightarrow * + O_2 + H^+ + e^- \quad (4)$$

Acknowledgements

We would like to acknowledge funding support from Singapore Ministry of Education Academic Research Fund (AcRF) Tier 1: RG10/16 and RG111/15, Tier 2: MOE2016-T2-2-004, and the National Key R&D Program of China (2016YFA0202804). J.L. acknowledges the financial support from National Natural Science Foundation of China (Nos. 21590792, 91645203, and 21521091).

Notes

Table S1-S3, Figure S1-S24 are provided in Supporting Information.

The authors declare no competing financial interests.

References

1. Seh, Z. W.; Kibsgaard, J.; Dickens, C. F.; Chorkendorff, I.; Norskov, J. K.; Jaramillo, T. F., Combining theory and experiment in electrocatalysis: Insights into materials design. *Science* **2017,** *355* (6321), 1-14.

2. Montoya, J. H.; Seitz, L. C.; Chakthranont, P.; Vojvodic, A.; Jaramillo, T. F.; Norskov, J. K., Materials for solar fuels and chemicals. *Nat. Mater.* **2016,** *16* (1), 70-81.

3. Carmo, M.; Fritz, D. L.; Merge, J.; Stolten, D., A comprehensive review on PEM water electrolysis. *Int. J. Hydrog. Energy* **2013,** *38* (12), 4901-4934.

4. Reier, T.; Nong, H. N.; Teschner, D.; Schlögl, R.; Strasser, P., Electrocatalytic oxygen evolution reaction in acidic environments - reaction mechanisms and catalysts. *Adv. Energy Mater.* **2017,** *7* (1), 1601275.

5. Spori, C.; Kwan, J. T. H.; Bonakdarpour, A.; Wilkinson, D. P.; Strasser, P., The stability challenges of oxygen evolving catalysts: Towards a common fundamental understanding and mitigation of catalyst degradation. *Angew. Chem. Int. Ed.* **2017,** *56* (22), 5994-6021.

6. Mondschein, J. S.; Callejas, J. F.; Read, C. G.; Chen, J. Y. C.; Holder, C. F.; Badding, C. K.; Schaak, R. E., Crystalline cobalt oxide films for sustained electrocatalytic oxygen evolution under strongly acidic conditions. *Chem. Mater.* **2017,** *29* (3), 950-957.

7. Danilovic, N.; Subbaraman, R.; Chang, K. C.; Chang, S. H.; Kang, Y. J. J.; Snyder, J.;

Paulikas, A. P.; Strmcnik, D.; Kim, Y. T.; Myers, D.; Stamenkovic, V. R.; Markovic, N. M., Activity-stability trends for the oxygen evolution reaction on monometallic oxides in acidic environments. *J. Phys. Chem. Lett.* **2014,** *5* (14), 2474-2478.

8. McCrory, C. C. L.; Jung, S.; Ferrer, I. M.; Chatman, S. M.; Peters, J. C.; Jaramillo, T. F., Benchmarking hydrogen evolving reaction and oxygen evolving reaction electrocatalysts for solar water splitting devices. *J. Am. Chem. Soc.* **2015,** *137* (13), 4347-4357.

9. Seitz, L. C.; Dickens, C. F.; Nishio, K.; Hikita, Y.; Montoya, J.; Doyle, A.; Kirk, C.; Vojvodic, A.; Hwang, H. Y.; Norskov, J. K.; Jaramillo, T. F., A highly active and stable $IrO_x/SrIrO_3$ catalyst for the oxygen evolution reaction. *Science* **2016,** *353* (6303), 1011-1014.

10. Lebedev, D.; Povia, M.; Waltar, K.; Abdala, P. M.; Castelli, I. E.; Fabbri, E.; Blanco, M. V.; Fedorov, A.; Copéret, C.; Marzari, N.; Schmidt, T. J., Highly active and stable iridium pyrochlores for oxygen evolution reaction. *Chem. Mater.* **2017,** *29* (12), 5182-5191.

11. Willinger, E.; Massue, C.; Schlogl, R.; Willinger, M. G., Identifying key structural features of IrO_x water splitting catalysts. *J. Am. Chem. Soc.* **2017,** *139* (34), 12093-12101.

12. Kim, J.; Shih, P.-C.; Tsao, K.-C.; Pan, Y.-T.; Yin, X.; Sun, C.-J.; Yang, H., High-performance pyrochlore-type yttrium ruthenate electrocatalyst for oxygen evolution reaction in acidic media. *J. Am. Chem. Soc.* **2017,** *139* (34), 12076-12083.

13. Kim, Y. T.; Lopes, P. P.; Park, S. A.; Lee, A. Y.; Lim, J.; Lee, H.; Back, S.; Jung, Y.; Danilovic, N.; Stamenkovic, V.; Erlebacher, J.; Snyder, J.; Markovic, N. M., Balancing activity, stability and conductivity of nanoporous core-shell iridium/iridium oxide oxygen evolution catalysts. *Nat. Commun.* **2017,** *8* (1), 1449.

14. Pfeifer, V.; Jones, T. E.; Velasco Velez, J. J.; Arrigo, R.; Piccinin, S.; Havecker, M.;

Knop-Gericke, A.; Schlogl, R., In situ observation of reactive oxygen species forming on oxygen-evolving iridium surfaces. *Chem. Sci.* **2017,** *8* (3), 2143-2149.

15. Pfeifer, V.; Jones, T. E.; Velasco Vélez, J. J.; Massué, C.; Arrigo, R.; Teschner, D.; Girgsdies, F.; Scherzer, M.; Greiner, M. T.; Allan, J.; Hashagen, M.; Weinberg, G.; Piccinin, S.; Hävecker, M.; Knop-Gericke, A.; Schlögl, R., The electronic structure of iridium and its oxides. *Surf. Interface Anal.* **2016,** *48* (5), 261-273.

16. Pfeifer, V.; Jones, T. E.; Velasco Velez, J. J.; Massue, C.; Greiner, M. T.; Arrigo, R.; Teschner, D.; Girgsdies, F.; Scherzer, M.; Allan, J.; Hashagen, M.; Weinberg, G.; Piccinin, S.; Havecker, M.; Knop-Gericke, A.; Schlogl, R., The electronic structure of iridium oxide electrodes active in water splitting. *Phys. Chem. Chem. Phys.* **2016,** *18* (4), 2292-2296.

17. Abbott, D. F.; Lebedev, D.; Waltar, K.; Povia, M.; Nachtegaal, M.; Fabbri, E.; Coperet, C.; Schmidt, T. J., Iridium oxide for the oxygen evolution reaction: Correlation between particle size, morphology, and the surface hydroxo layer from operando XAS. *Chem. Mater.* **2016,** *28* (18), 6591-6604.

18. Massue, C.; Huang, X.; Tarasov, A.; Ranjan, C.; Cap, S.; Schlogl, R., Microwave-assisted synthesis of stable and highly active ir oxohydroxides for electrochemical oxidation of water. *ChemSusChem* **2017,** *10* (9), 1958-1968.

19. Karimi, F.; Bazylak, A.; Peppley, B. A., Effect of calcination temperature on the morphological and electrochemical characteristics of supported iridium hydroxyoxide electrocatalysts for the pem electrolyzer anode. *J. Electrochem. Soc.* **2017,** *164* (4), F464-F474.

20. Ooka, H.; Wang, Y. Q.; Yamaguchi, A.; Hatakeyama, M.; Nakamura, S.; Hashimoto, K.;

Nakamura, R., Legitimate intermediates of oxygen evolution on iridium oxide revealed by in situ electrochemical evanescent wave spectroscopy. *Phys. Chem. Chem. Phys.* **2016,** *18* (22), 15199-15204.

21. Sanchez Casalongue, H. G.; Ng, M. L.; Kaya, S.; Friebel, D.; Ogasawara, H.; Nilsson, A., In situ observation of surface species on iridium oxide nanoparticles during the oxygen evolution reaction. *Angew. Chem. Int. Ed.* **2014,** *53* (28), 7169-7172.

22. Lyons, M. E. G.; Floquet, S., Mechanism of oxygen reactions at porous oxide electrodes. Part 2-Oxygen evolution at RuO_2, IrO_2 and $Ir_xRu_{1-x}O_2$ electrodes in aqueous acid and alkaline solution. *Phys. Chem. Chem. Phys.* **2011,** *13* (12), 5314-5335.

23. Pavlovic, Z.; Ranjan, C.; van Gastel, M.; Schlogl, R., The active site for the water oxidising anodic iridium oxide probed through in situ Raman spectroscopy. *Chem. Commun.* **2017,** *53* (92), 12414-12417.

24. Grimaud, A.; Demortiere, A.; Saubanere, M.; Dachraoui, W.; Duchamp, M.; Doublet, M.-L.; Tarascon, J.-M., Activation of surface oxygen sites on an iridium-based model catalyst for the oxygen evolution reaction. *Nat. Energy* **2016,** *2* (1), 16189.

25. Korotcov, A. V.; Huang, Y. S.; Tiong, K. K.; Tsai, D. S., Raman scattering characterization of well-aligned RuO_2 and IrO_2 nanocrystals. *J. Raman Spectrosc.* **2007,** *38* (6), 737-749.

26. Freakley, S. J.; Ruiz-Esquius, J.; Morgan, D. J., The X-ray photoelectron spectra of Ir, IrO_2 and $IrCl_3$ revisited. *Surf. Interface Anal.* **2017,** *49* (8), 794-799.

27. Shan, C. C.; Tsai, D. S.; Huang, Y. S.; Jian, S. H.; Cheng, C. L., Pt-Ir-IrO_2NT thin-wall electrocatalysts derived from IrO_2 nanotubes and their catalytic activities in methanol

oxidation. *Chem. Mater.* **2007,** *19* (3), 424-431.

28. Kodintsev, I. M.; Trasatti, S.; Rubel, M.; Wieckowski, A.; Kaufher, N., X-ray photoelectron-spectroscopy and electrochemical surface characterization of IrO_2 + RuO_2 electrodes. *Langmuir* **1992,** *8* (1), 283-290.

29. Zhao, S.; Yu, H.; Maric, R.; Danilovic, N.; Capuano, C. B.; Ayers, K. E.; Mustain, W. E., Calculating the electrochemically active surface area of iridium oxide in operating proton exchange membrane electrolyzers. *J. Electrochem. Soc.* **2015,** *162* (12), 1292-1298.

30. Rakousky, C.; Shviro, M.; Carmo, M.; Stolten, D., Iridium nanoparticles for the oxygen evolution reaction: Correlation of structure and activity of benchmark catalyst systems. *Electrochim. Acta* **2018**, in press, doi: 10.1016/j.electacta.2018.11.141.

31. Alia, S. M.; Rasimick, B.; Ngo, C.; Neyerlin, K. C.; Kocha, S. S.; Pylypenko, S.; Xu, H.; Pivovar, B. S., Activity and durability of iridium nanoparticles in the oxygen evolution reaction. *J. Electrochem. Soc.* **2016,** *163* (11), 3105-3112.

32. Alia, S. M.; Hurst, K. E.; Kocha, S. S.; Pivovar, B. S., Mercury underpotential deposition to determine iridium and iridium oxide electrochemical surface areas. *J. Electrochem. Soc.* **2016,** *163* (11), 3051-3056.

33. Godínez-Salomón, F.; Albiter, L.; Alia, S. M.; Pivovar, B. S.; Camacho-Forero, L. E.; Balbuena, P. B.; Mendoza-Cruz, R.; Arellano-Jimenez, M. J.; Rhodes, C. P., Self-supported hydrous iridium–nickel oxide two-dimensional nanoframes for high activity oxygen evolution electrocatalysts. *ACS Catal.* **2018,** *8* (11), 10498-10520.

34. Massue, C.; Pfeifer, V.; Huang, X.; Noack, J.; Tarasov, A.; Cap, S.; Schlogl, R., High-performance supported iridium oxohydroxide water oxidation electrocatalysts.

ChemSusChem **2017,** *10* (9), 1943-1957.

35. Reier, T.; Oezaslan, M.; Strasser, P., Electrocatalytic oxygen evolution reaction (OER) on Ru, Ir, and Pt catalysts: A comparative study of nanoparticles and bulk materials. *ACS Catal.* **2012,** *2* (8), 1765-1772.

36. Jovanovic, P.; Hodnik, N.; Ruiz-Zepeda, F.; Arcon, I.; Jozinovic, B.; Zorko, M.; Bele, M.; Sala, M.; Selih, V. S.; Hocevar, S.; Gaberscek, M., Electrochemical dissolution of iridium and iridium oxide particles in acidic media: Transmission electron microscopy, electrochemical flow cell coupled to inductively coupled plasma mass spectrometry, and x-ray absorption spectroscopy study. *J. Am. Chem. Soc.* **2017,** *139* (36), 12837-12846.

37. Cahan, B. D.; Chen, C. T., Questions on the kinetics of O_2 evolution on oxide-covered metals. *J. Electrochem. Soc.* **1982,** *129* (4), 700-705.

38. Lyons, M. E. G.; Brandon, M. P., The significance of electrochemical impedance spectra recorded during active oxygen evolution for oxide covered Ni, Co and Fe electrodes in alkaline solution. *J. Electroanal. Chem.* **2009,** *631* (1-2), 62-70.

39. Grahame, D. C., The electrical double layer and the theory of electrocapillarity. *Chem. Rev.* **1947,** *41* (3), 441-501.

40. Hillman, A. R.; Skopek, M. A.; Gurman, S. J., X-Ray spectroscopy of electrochemically deposited iridium oxide films: detection of multiple sites through structural disorder. *Phys. Chem. Chem. Phys.* **2011,** *13* (12), 5252-5263.

41. Minguzzi, A.; Lugaresi, O.; Achilli, E.; Locatelli, C.; Vertova, A.; Ghigna, P.; Rondinini, S., Observing the oxidation state turnover in heterogeneous iridium-based water oxidation catalysts. *Chem. Sci.* **2014,** *5* (9), 3591.

42. Grimaud, A.; Hong, W. T.; Shao-Horn, Y.; Tarascon, J. M., Anionic redox processes for electrochemical devices. *Nat. Mater.* **2016,** *15* (2), 121-126.

43. Ooka, H.; Yamaguchi, A.; Takashima, T.; Hashimoto, K.; Nakamura, R., Efficiency of oxygen evolution on iridium oxide determined from the pH dependence of charge accumulation. *J. Phys. Chem. C* **2017,** *121* (33), 17873-17881.

44. Doyle, R. L.; Lyons, M. E. G., The oxygen evolution reaction: Mechanistic concepts and catalyst design. In *Photoelectrochemical Solar Fuel Production: From Basic Principles to Advanced Devices*, Giménez, S.; Bisquert, J., Eds. Springer International Publishing: Cham, 2016; 41-104.

45. Hu, J.-M.; Zhang, J.-Q.; Cao, C.-N., Oxygen evolution reaction on IrO_2-based DSA® type electrodes: kinetics analysis of Tafel lines and EIS. *Int. J. Hydrog. Energy* **2004,** *29* (8), 791-797.

46. Ping, Y.; Nielsen, R. J.; Goddard, W. A., III, The reaction mechanism with free energy barriers at constant potentials for the oxygen evolution reaction at the IrO_2 (110) surface. *J. Am. Chem. Soc.* **2017,** *139* (1), 149-155.

47. Man, I. C.; Su, H.-Y.; Calle-Vallejo, F.; Hansen, H. A.; Martínez, J. I.; Inoglu, N. G.; Kitchin, J.; Jaramillo, T. F.; Nørskov, J. K.; Rossmeisl, J., Universality in oxygen evolution electrocatalysis on oxide surfaces. *ChemCatChem* **2011,** *3* (7), 1159-1165.

48. Rossmeisl, J.; Qu, Z. W.; Zhu, H.; Kroes, G. J.; Nørskov, J. K., Electrolysis of water on oxide surfaces. *J. Electroanal. Chem.* **2007,** *607* (1-2), 83-89.

49. Gauthier, J. A.; Dickens, C. F.; Chen, L. D.; Doyle, A. D.; Nørskov, J. K., Solvation effects for oxygen evolution reaction catalysis on IrO_2(110). *J. Phys. Chem. C* **2017,** *121* (21),

11455-11463.

50. Exner, K. S.; Over, H., Kinetics of electrocatalytic reactions from first-principles: A critical comparison with the ab initio thermodynamics approach. *Acc. Chem. Res.* **2017,** *50* (5), 1240-1247.

51. Shinagawa, T.; Garcia-Esparza, A. T.; Takanabe, K., Insight on Tafel slopes from a microkinetic analysis of aqueous electrocatalysis for energy conversion. *Sci. Rep.* **2015,** *5*, 13801.

52. Bockris, J. O.; Otagawa, T., Mechanism of oxygen evolution on perovskites. *J. Phys. Chem.* **1983,** *87* (15), 2960-2971.

53. Kresse, G.; Furthmüller, J., Efficient iterative schemes for ab initio total-energy calculations using a plane-wave basis set. *Phys. Rev. B* **1996,** *54* (16), 11169-11186.

54. Kresse, G.; Furthmüller, J., Efficiency of ab-initio total energy calculations for metals and semiconductors using a plane-wave basis set. *Comput. Mater. Sci.* **1996,** *6* (1), 15-50.

55. Blöchl, P. E., Projector augmented-wave method. *Phys. Rev. B* **1994,** *50* (24), 17953-17979.

56. Perdew, J. P.; Burke, K.; Ernzerhof, M., Generalized gradient approximation made simple. *Phys. Rev. Lett.* **1996,** *77* (18), 3865-3868.

57. Monkhorst, H. J.; Pack, J. D., Special points for Brillouin-zone integrations. *Phys. Rev. B* **1976,** *13* (12), 5188-5192.

58. Bolzan, A. A.; Fong, C.; Kennedy, B. J.; Howard, C. J., Structural studies of rutile-type metal dioxides. *Acta Crystallogr., Sect. B* **1997,** *53* (3), 373-380.

59. Fang, Y.-H.; Liu, Z.-P., Mechanism and tafel lines of electro-oxidation of water to

oxygen on RuO_2(110). *J. Am. Chem. Soc.* **2010,** *132* (51), 18214-18222.

For Table of Contents Only